Accepted Manuscript

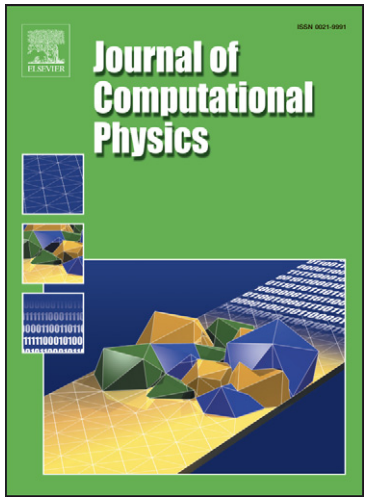

A comparative study of interface reconstruction methods for multi-material ALE simulations

Milan Kucharik, Rao V. Garimella, Samuel P. Schofield, Mikhail J. Shashkov

PII: S0021-9991(09)00389-1
DOI: 10.1016/j.jcp.2009.07.009
Reference: YJCPH 2671

To appear in: *Journal of Computational Physics*

Received Date: 9 March 2009
Revised Date: 3 July 2009
Accepted Date: 13 July 2009

Please cite this article as: M. Kucharik, R.V. Garimella, S.P. Schofield, M.J. Shashkov, A comparative study of interface reconstruction methods for multi-material ALE simulations, *Journal of Computational Physics* (2009), doi: 10.1016/j.jcp.2009.07.009

This is a PDF file of an unedited manuscript that has been accepted for publication. As a service to our customers we are providing this early version of the manuscript. The manuscript will undergo copyediting, typesetting, and review of the resulting proof before it is published in its final form. Please note that during the production process errors may be discovered which could affect the content, and all legal disclaimers that apply to the journal pertain.

ACCEPTED MANUSCRIPT

A comparative study of interface reconstruction methods for multi-material ALE simulations

Milan Kucharik

Applied Math and Plasma Physics (T-5), Los Alamos National Laboratory

Rao V. Garimella

Applied Math and Plasma Physics (T-5), Los Alamos National Laboratory

Samuel P. Schofield

Applied Math and Plasma Physics (T-5), Los Alamos National Laboratory

Mikhail J. Shashkov

Applied Math and Plasma Physics (T-5), Los Alamos National Laboratory

Abstract

In this paper we compare the performance of different methods for reconstructing interfaces in multi-material compressible flow simulations. The methods compared are a material-order-dependent Volume-of-Fluid (VOF) method, a material-order-independent VOF method based on power diagram partitioning of cells and the Moment-of-Fluid method (MOF). We demonstrate that the MOF method provides the most accurate tracking of interfaces, followed by the VOF method with the right material ordering. The material-order-independent VOF method performs somewhat worse than the above two while the solutions with VOF using the wrong material order are considerably worse.

Key words:
Interface Reconstruction, Moment-of-fluid method, compressible flow

Email addresses: kucharik@lanl.gov, kucharik@karkulka.fjfi.cvut.cz (Milan Kucharik), rao@lanl.gov (Rao V. Garimella), sams@lanl.gov (Samuel P. Schofield), shashkov@lanl.gov (Mikhail J. Shashkov).

ACCEPTED MANUSCRIPT

1 Introduction

Accurate simulation of multi-material and multi-phase flows requires effective tracking and management of material interfaces. Due to their ability to strictly conserve the mass of different materials, volume-of-fluid (VOF) methods using interface reconstruction are widely used in such simulations [1–4]. Originally developed by Hirt and Nichols [5], VOF methods do not explicitly track interfaces but rather track the volume of each material. The interface between materials is first reconstructed in cells based on the material volume fractions. Then the volume fluxes of each material between cells are estimated from the geometric reconstruction and finally, the fluxes are used to compute new volume fractions in each cell, in preparation for the next time step.

More recently, an interface tracking method has been devised based on tracking both the volume (zeroth moment) and centroid (ratio of first and zeroth moment) of the materials in mesh cells. This new method, called the Moment-of-Fluid (MOF) method [6], reconstructs interfaces more accurately than VOF methods and is able to resolve interfacial features on the order of the local mesh size whereas VOF methods do poorly in resolving features smaller than 3-4 times the local mesh size.

In this paper, we present a comparative study of different VOF methods and the MOF method for complex compressible flow simulations involving more than two materials. It is organized as follows: in Section 2, we present a brief overview of the common material order-dependent VOF methods. We describe the basic principle of each method and focus mainly on the Youngs' VOF method, which is implemented in most multi-material codes. We describe the problems with choosing the correct material ordering for such methods. In Section 3, we describe the order independent VOF method based on the power diagrams. In Section 4, the MOF material reconstruction method is described. The slope of the material interface is not determined from the volume fractions of the neighboring cells, but from the material centroids of the particular cell. In Section 5, we briefly describe all steps of the ALE algorithm implemented in our research multi-material code. We focus mainly on the propagation of the material centroids needed for the MOF material reconstruction during the Lagrangian and remapping steps of the algorithm. Coupling of the material reconstruction methods with a multi-material ALE code is described. Section 6 is the key part of the paper. It includes comparison of the described material reconstruction methods in the context of particular multi-material hydrodynamic simulations including typical phenomena appearing in real problems – vortex, explosion, and a shock wave-material interaction. All numerical examples include more than 2 materials to emphasize key properties of each method. Finally, we conclude the paper and review the material reconstruction methods in Section 7.

ACCEPTED MANUSCRIPT

2 VOF Methods with Nested Dissection (VOF-PLIC)

Early VOF methods used a straight line aligned with a coordinate axis to partition the cell according to the material volume fractions. This is often referred to as the simple line interface calculation (SLIC) originally due to Noh and Woodward [7]. Youngs [8,9] extended the method to permit the material interface to have an arbitrary orientation within the cell (called PLIC or Piecewise Linear Interface Calculation by Rider and Kothe [3]). In Youngs' method, the outward normal of the interface separating a material from the rest of the cell is taken to be the negative gradient of the "volume fraction function". The "volume fraction function" is treated as a smooth function whose cell-centered values are given by the cell-wise material volume fractions. The interface is then defined by locating a line with the prescribed normal that cuts off the correct volume of material from the computational cell.

Gradient based methods are in general first order accurate although they may exhibit near second order accuracy on regular Cartesian grids. However, there are extensions that make the reconstruction second-order accurate for general grids. The LVIRA technique by Pilliod and Puckett [10] tries to find an extended straight line interface that cuts off the exact volume fraction in the cell of interest and minimizes the error in matching the volume fractions in the surrounding cells. LVIRA uses a minimization procedure with a gradient-based normal as the initial guess. An alternative is the interface smoothing procedure based on Swartz's quadratically convergent procedure [11] for finding a straight line that cuts off the right volume fractions from two arbitrary planar shapes [1] . Mosso et.al [14] and Garimella et.al. [15] have used this procedure in slightly different ways to devise interface smoothing procedures. For a given mixed cell, Garimella et.al. compute a straight line cutting off the right volume fractions from the cell and each of its mixed cell neighbors by the Swartz method. The normals of these different straight lines are then averaged to give a smoothed interface normal for the cell.

VOF-PLIC techniques have been successfully used to accurately simulate two-phase (or two-material) flows and free-surface flows in two and three dimensions. However, their application to flows involving three or more materials that come closer than the mesh spacing and even form junctions has been mostly *ad hoc*. Examples of such phenomena are flows of immiscible fluids (*e.g.* oil-water-gas), inertial confinement fusion, armor-antiarmor penetration and powder metallurgical simulation of multiple materials.

The most common extensions of PLIC to cells with more than two materials

[1] This is commonly known as the "ham-sandwich" or Steinhaus problem[12,13]

ACCEPTED MANUSCRIPT

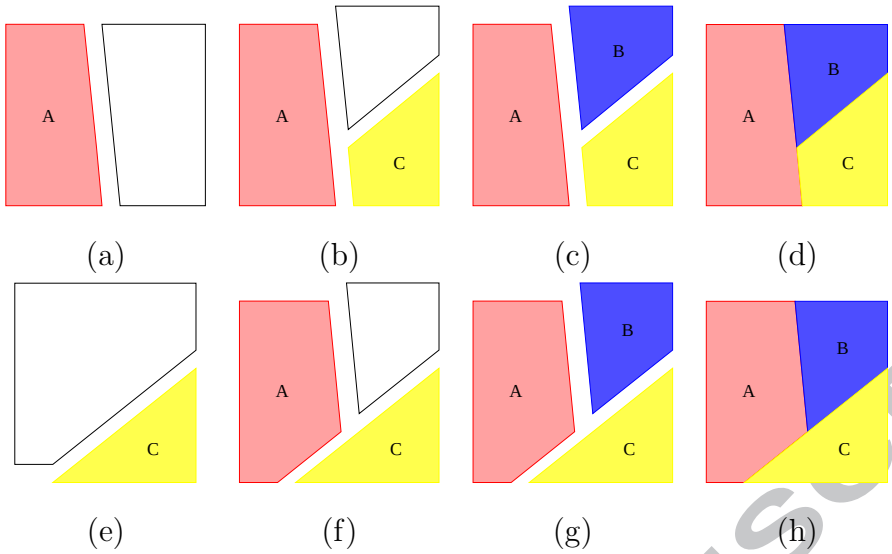

Fig. 1. Nested dissection interface reconstruction for three materials in the order ACB: (a) the first (A) material is removed leaving a smaller available polygon, (b) the second (C) material is removed from the available polygon, (c) the remaining available polygon is assigned to material B, (d) the resulting partitioning of the computational cell. (e)-(g) show the same procedure but the materials are processed in a different (CAB) order leading to a different reconstruction (h).

(multi-material cells) [2], is to process materials one by one leading to a reconstruction that is strongly dependent on the order in which the materials are processed. Of the different ways to sequentially partition a cell, one of the most general and accurate ways is called the "nested dissection" method [6], where each material is separated from the others in a specified order. In the method, a pure polygon (or polyhedron) representing the first material is marked out from the cell, leaving a mixed polygon for the remaining materials. Then, a polygon representing the second material is marked out from the mixed polygon and the process continues until the last material is processed. This method is illustrated in Figure 1 and described in detail in [6,16,17]. Clearly, such an order dependent method can easily place materials in wrong locations in the cells if the chosen order of processing is incorrect. Even if the order of the materials is right, the computation of the interface normals in multi-material cells is ambiguous. In computing the normal as the negative gradient of the volume fraction function of a material, it is unclear whether one should use the volume fractions with respect to original cells or the part of the cells remaining after the earlier materials have been removed. It is also

[2] In a strict sense, any cell with more than one material is a multi-material cell. However, we choose to distinguish two material cells from cells with more than two materials by calling the latter multi-material cells. The reason for this distinction is that interface reconstruction for one material is (in the case of VOF methods) complementary to the second in a cell with two-materials while it is not for more than two materials

ACCEPTED MANUSCRIPT

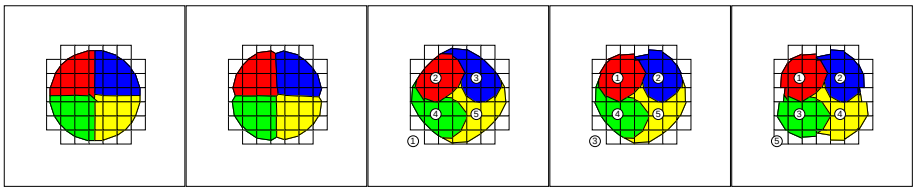

Fig. 2. Four material disk at time $T = 0.5$ translated from the initial position $(0.2, 0.2)$ with 30 time steps at a velocity of $(1, 1)$ on 32×32 mesh of the $[0, 1]^2$ domain. Material reconstruction done by several methods – MOF, VOF with power diagrams, and Youngs' VOF. The material orderings for Youngs' are indicated in the figure.

not clear where these function values should be centered – at the center of the original cell or the center of the unprocessed part of the cell.

The most significant adverse effect of these incorrect reconstructions, however, is in material advection in flow simulations. An improper material ordering may result in materials being advected prematurely (or belatedly) into neighboring cells. This can further lead to small pieces of the material getting separated and drifting away from the bulk of the material (sometimes known as "flotsam and jetsam"). The effect of material ordering is illustrated clearly in an example from [18] in which a four-material disk (with each material occupying one quadrant of the disk) is advected diagonally for 30 time steps. The results in Figure 2 show dramatically different results with different material orderings and a complete loss of the cross-shaped interface.

The most common and trivial way to deal with the material order dependency is to select the "correct" global ordering for a problem. However, this is obviously problematic if the same materials must be processed differently in different parts of the mesh or if the material configurations change as the problem advances in time. Also, some interface configurations may not be reproducible by any particular order, such as the four material example referred to above. While there has been some work on automatically deriving material order, most of these attempts assume a layered structure for the interface [14,19] and cannot handle multiple materials coming together at a point very well.

3 VOF Methods with Power Diagram Reconstruction (VOF-PD)

Recently, Schofield et. al. [18] developed a new VOF-based reconstruction method that is completely material order independent. This method, called the Power Diagram method for Interface Reconstruction, does not sequentially carve off materials from a cell using straight lines. Rather it first lo-

ACCEPTED MANUSCRIPT

cates materials approximately in multi-material cells and then partitions the cell simultaneously into multiple material regions using a weighted Voronoi decomposition thereby avoiding the order dependence problem. We describe this procedure below referring to it as the VOF-PD method.

In the first step of the VOF-PD method, approximate locations or "centroids" of the materials in a cell are determined using the volume fractions of the materials in the cell and its neighbors. This is accomplished by treating the volume fractions of each material in the cell and its neighbors as pointwise values of a pseudo-density function. The pointwise values of this pseudo-density function are then used to obtain a linear reconstruction of the function along with application of a limiter restricting the minimum and maximum values to 0 and 1 respectively. Then the linear approximation of this pseudo-density function is used to derive an approximate centroid for the material in the cell. While this method does not locate the material centroids very accurately in an absolute sense, it does locate the materials quite well relative to each other.

In the second step of the procedure, the approximate centroids of the materials are used as generators for a weighted Voronoi or Power Diagram subdivision [20,21] of the cell. The weights of the different generators are chosen iteratively such that the volume fractions of the different Voronoi polygons truncated by the cell boundary match the specified material volume fractions exactly.

The authors have shown that this procedure is in general first-order accurate and for two materials, exactly reproduces a gradient-based subdivision of the cell. They have also presented a smoothing procedure for the power diagram-based subdivision which results in a second-order accurate reconstruction but slows the procedure down considerably unless applied only to cells with more than two materials.

4 Moment-of-Fluid (MOF) Method

While VOF methods track only volume fractions of the individual materials in mesh cells, the recently developed Moment-of-Fluid (MOF) method [6] tracks both the volume (zeroth moment) and centroid (ratio of first and zeroth moment) of the materials in the cells. By tracking both moments the MOF method reconstructs the material interface with higher accuracy than VOF methods and is able to resolve interfacial details on the order of the local mesh size. In contrast, VOF methods can only resolve details on the order of 3-4 times the local mesh size. Also, since a line can be determined by only two parameters (an intercept and a slope), the linear interface in a cell is actually over-determined by specifying the volume fraction and centroid. This implies that MOF can perform an exact reconstruction of a linear interface and a

ACCEPTED MANUSCRIPT

second-order reconstruction of a smoothly curved interface in a cell without the need for information from neighboring cells.

Given the volume fraction and centroid of a material in a cell, the MOF reconstruction method computes a linear interface such that the volume fraction of the material is exactly matched and the discrepancy between the specified centroid and the centroid of the polygon or polyhedron behind interface is minimized. This is done by an optimization process with the slope of the linear interface (or its angle with respect to the x-direction) as the primary variable. For any given slope, the intercept of the line is determined uniquely by matching the specified material volume fraction.

The MOF reconstruction is also typically implemented as a nested dissection method where materials are carved off from a cell sequentially thereby making it an order-dependent problem. However, it is possible to combinatorially determine the correct sequence of material reconstructions in MOF by reconstructing with all possible sequences and choosing the sequence which leads to the least discrepancy between the reconstruction and specified centroids. Although the number of possible sequences grows as the factorial of the number of materials, the computational overhead of this approach is tolerable as each cell contains only a small number of materials for most problems. Also, more complex configurations such as 4 materials coming together at a point can be reconstructed by recursively reconstructing the interface between groups of materials first and then resolving the interfaces between materials in each group. Again, due to the small number of materials in a cell, this does not impose a significant computational penalty. Such a technique has proved very effective in accurately reconstructing multi-material interfaces.

Further details of the MOF technique of interface reconstruction are given in [6,17].

5 Compressible flow simulation with VOF and MOF reconstructions

Here we briefly describe an arbitrary-Eulerian-Lagrangian (ALE) compressible flow simulation algorithm used to compare the effects of the VOF and MOF reconstruction techniques. Since the purpose of this paper is to compare the different interface reconstruction methods, we deliberately do not provide many details of the ALE code to avoid overwhelming the discussion. We believe the general conclusions of this comparative study will hold regardless of the ALE code used.

Our 2D research multi-material ALE code (RMALE) has a standard struc-

ACCEPTED MANUSCRIPT

ture shown in Figure 3. It consists of three main components – multi-material

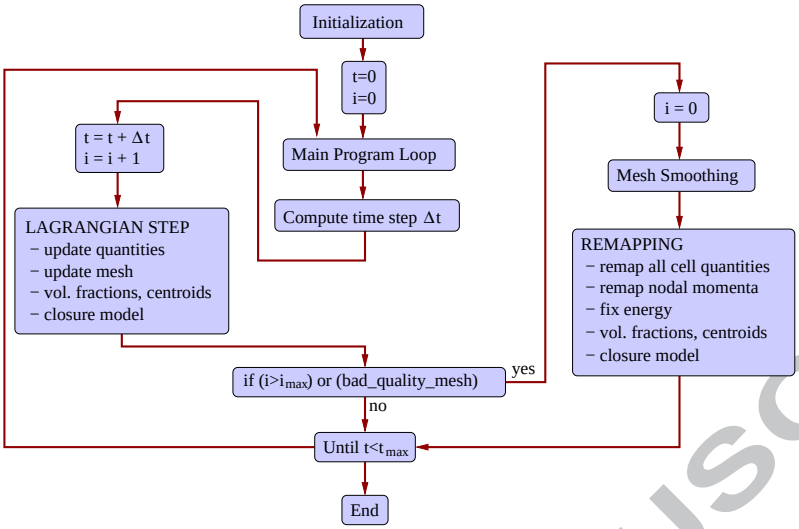

Fig. 3. Flowchart of our research multi-material code. Material reconstruction is hidden in the update of material centroids at the end of the Lagrangian step.

Lagrangian solver, mesh untangling and smoothing method, and a flux-based multi-material remapper. The Lagrangian step is repeated, until the mesh smoothing becomes necessary (for example, due to poor mesh quality, or a given number of hydro steps being completed). When mesh smoothing is applied to improving the mesh quality it is followed by a remapping step conservatively interpolating all quantities on the new mesh. Then, a new Lagrangian cycle can begin. The entire code employs a staggered Mimetic Finite Difference discretization [22], where scalar fluid quantities (density, mass, pressure, internal energy) are located inside mesh cells, and vector quantities (positions, velocities) on mesh nodes. The multi-material ALE framework allows more than one material inside one computational cell, where the amount of each material is defined by its volume and mass fractions, and if we use MOF, the relative location of each material is defined by the material centroid. In each multi-material cell, scalar quantities are defined separately for every material, but the variables in the primary equations are the average cell quantities. Contrary to a single-material approach, our multi-material Lagrangian step and remapper must update not only all fluid quantities, but also material volume and mass fractions, and material centroids.

The Lagrangian solver solves the following set of hydrodynamic equations

$$\frac{1}{\rho}\frac{d\rho}{dt} = -\nabla\cdot\mathbf{w}\,, \quad \rho\frac{d\mathbf{w}}{dt} = -\nabla\cdot p\,, \quad \rho\frac{d\varepsilon}{dt} = -p\,\nabla\cdot\mathbf{w} \tag{1}$$

representing conservation of mass, momenta in both directions, and total energy, completed by the ideal gas equation of state $p = (\gamma-1)\,\rho\,\varepsilon$. Here, ρ is the fluid density, $\mathbf{w}$ is the vector of velocities, p is the fluid pressure, ε is the specific

ACCEPTED MANUSCRIPT

internal energy, and γ is the ratio of specific heats. The solver is based on evaluation of several types of forces affecting each mesh node [22] – zonal pressure force representing forces due to the pressure in all neighboring zones, artificial viscosity force (edge viscosity [23] is used in the examples), and anti-hourglass stabilization force introduced in [24], suppressing some unphysical modes in the mesh motion. The viscosity forces in the mixed cells are computed from the average fluid quantities, and the appropriate heating is redistributed among the particular materials according to their mass fractions. For volume fraction update and common pressure construction, a multi-material closure model is applied [25]. In our numerical examples, the simplest model employing the constant volume fractions (equal strain model [1]), is used. The last part of the Lagrangian step is a method for updating the material centroids. In the first step, we advect them by keeping their parametric coordinates constant. Appendix A shows that this method reproduces the Lagrangian motion of the centroid for compressible flows with second-order accuracy. These centroids are then used (together with updated volume fractions) as reference centroids for the next material reconstruction step. The final material centroids are then set to the centroids of the reconstructed polygons.

Our code incorporates several mesh-untangling and mesh-smoothing methods. All ALE examples in this paper use one iteration of the classical Winslow mesh smoothing algorithm [26] performed in a Jacobi manner to avoid breaking the problem symmetry.

The last essential part of the ALE code is a remapping technique interpolating all fluid and material quantities between Lagrangian and smoothed computational meshes. Our remapper employs the cell-cell or pure polygon-cell intersections and exact integration in the entire mesh, performed in a flux form. This flux-based remapper represents the multi-material extension of the technique described in [27] – it constructs inward and outward fluxes of integrals of 1, x, y, and some higher order polynomials using overlays (intersections) of Lagrangian cells (or pure material polygons in the case of mixed cells) with their neighbors in the smoothed mesh, and vice versa. Note that these integrals of polynomials over polygons can be computed analytically. Fluxes of all cell- and material-centered quantities are then constructed from these precomputed exchange integrals, the material quantities (mass, internal energy) are remapped in a material-by-material way. They are also used for remapping material volumes (and consequently volume fractions) and centroids in a flux form. For remapping nodal mass, we need to construct inter-nodal mass fluxes, which we interpolate from inter-cell mass fluxes as described in [28], extended by split side fluxes for adjacent cells and corner fluxes. All nodal quantities are then remapped by attaching them to these inter-nodal mass fluxes (for example, the momentum fluxes are obtained by multiplication of the mass fluxes by an interpolated flux velocity). This approach allows us to construct two kinetic energies at each node – conservative kinetic energy obtained by its

ACCEPTED MANUSCRIPT

remap, and non-conservative kinetic energy obtained from remapped velocities. This kinetic energy discrepancy is resolved by a standard energy fix [1], it is redistributed into the remapped internal energy of adjacent materials, and thus global energy conservation is guaranteed. For a complete detailed description of our multi-material remapping method, see [29].

The material reconstruction method is performed at the end of the Lagrangian stage, during the centroid update process. This whole step can be avoided when VOF type of method is used, and no centroid information is required. The second part of the ALE algorithm employing the material reconstruction method is the beginning of the remapping stage, during the computation of the material exchange integrals, and can also be reused during the slope (of density or internal energy) limiting. This material reconstruction must be performed in every remapping step, independent of the reconstruction method used, or the data from the Lagrangian step reconstruction can be reused, if it was performed.

6 Numerical examples

We demonstrate the properties of the described material reconstruction methods in the context of multi-material ALE hydrocode for three types of problems. These are: a triple point problem containing a strong vortex in its solution, a multi-material modification of the Sedov problem representing a material expansion (and thus its narrowing) due to a point explosion, and finally a multi-material modification of Saltzman problem employing the interaction of the piston-generated shock wave with a multi-material structure. These three problems represent a wide range of processes involved in real complex numerical hydro simulations. In our comparison, we focus especially on the material topology (relative position of the materials) and on how well the thin material filaments are resolved.

6.1 Triple point problem

The initial data for the triple point problem is shown in Figure 4. The computational domain has a rectangular shape with 7×3 edge ratio. In all simulations, we use an equispaced orthogonal initial computational mesh with 140×60 cells. It includes three materials at rest, initially forming a T-junction. The high-pressure material (in light red or white) creates a shock wave moving to to the right, through the low pressure blue (or darkest gray) and green (medium gray) materials. Due to different material properties, it moves faster in the blue or dark gray (lower density) material, and therefore a vortex evolves

ACCEPTED MANUSCRIPT

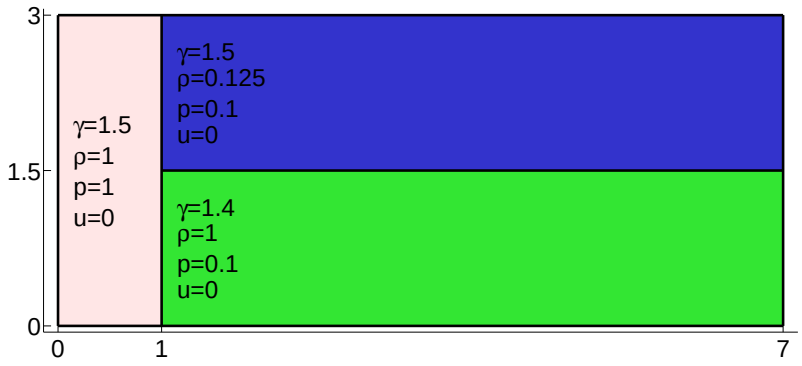

Fig. 4. Initial conditions for static triple point problem. Materials are shown in different colors, and values of ratio of specific heats γ, density ρ, pressure p, and velocity u are listed.

around the triple point. In the later stages of the simulation (final time $T = 5$), we can observe thin filaments of materials rotating around the vortex. It is to be noted that no mixed cells are present at the beginning of the simulations, however, they appear during the first remap.

Here, we compare a traditional gradient-based VOF method with different orderings, the MOF method, and a VOF method based on power diagrams (VOF-PD). We perform the comparison for two types of simulations: Eulerian and full ALE. In the Eulerian approach, the solution is remapped back to the orthogonal initial mesh after each Lagrangian step, while in the ALE approach, Winslow mesh smoothing and consecutive remapping is performed after every 20 Lagrangian steps.

In Figure 5, we can see the first snapshot of the Eulerian simulation, corresponding to time $T = 0.1$. In this early moment, the white-blue interface is shifted more to the right than the white-green one. As we can see, smooth interfaces are preserved when using VOF starting with white material, which is the correct local material ordering for this particular problem, and when using the MOF method. The VOF with Power diagrams still provide acceptable results, while VOF methods using wrong orderings created very distorted interfaces leading to problems in later stages of the simulation.

A snapshot in the middle of the simulation ($T = 2.5$) is shown in Figure 6. A thin filament of green material is starting to develop, which is reasonably resolved using MOF and VOF with the correct ordering. VOF with power diagrams keeps the correct topology of materials, but starts to have problems with resolving the thin filament. VOF with the wrong material orderings provides the worst results – the filament starts to separate from the heavy blue material, and there are small pieces of white material between green and blue that are not easily visible at this scale.

In Figure 7, we can see the final snapshot of the Eulerian simulation corre-

ACCEPTED MANUSCRIPT

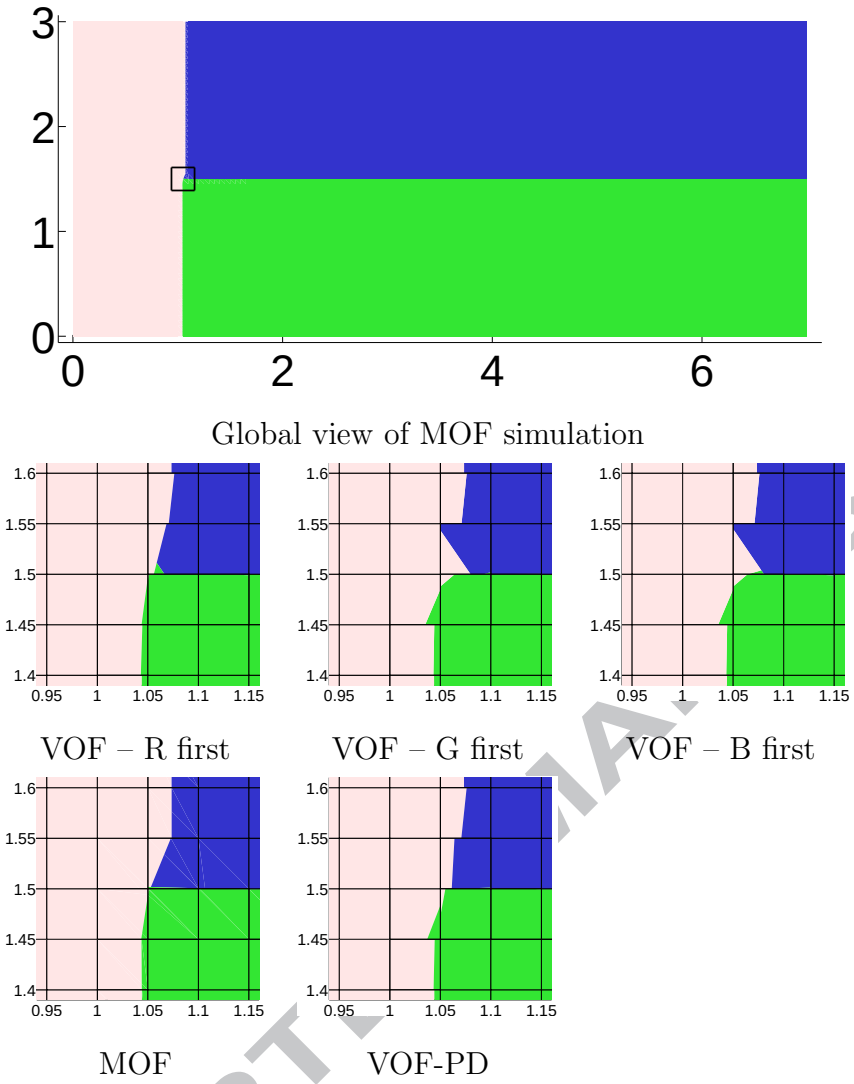

Fig. 5. Materials of triple point problem simulation, time $T = 0.1$. Eulerian runs (as Lagrangian step and remap to the initial orthogonal mesh) using different methods for material reconstruction are shown: global view on the entire computational domain for MOF method, and zooms to the three material junction for Youngs' VOF method (with different material orderings), MOF, and Power Diagram based methods are shown.

sponding to time $T = 5$. Again, MOF and VOF in the correct ordering resolve the thin part of the green filament reasonably well. VOF with the wrong material orderings give us unacceptable results – filament transforms into a drip separating from the blue material, and there are many tiny droplets of white material between the blue and green materials VOF with power diagrams also do not succeed in resolving the thin part of the filament, but the result is qualitatively better: the material topology is correct, no droplets appear, and green material stays attached to the blue one.

In the next set of figures, the results of the same problem obtained by ALE

ACCEPTED MANUSCRIPT

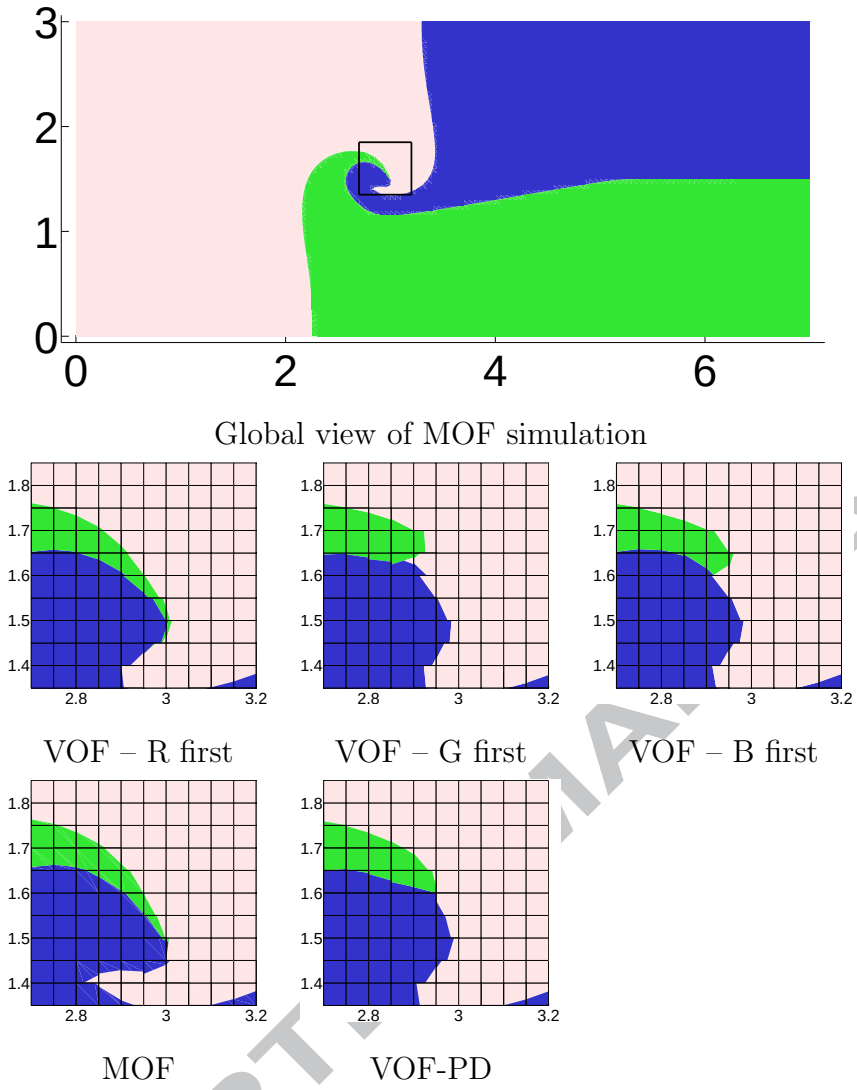

Fig. 6. Materials of triple point problem simulation, time $T = 2.5$. Eulerian runs (as Lagrangian step and remap to the initial orthogonal mesh) using different methods for material reconstruction are shown: global view on the entire computational domain for MOF method, and zooms to the three material junction for Youngs' VOF method (with different material orderings), MOF, and Power Diagram based methods are shown.

approach are presented. Generally, the results are worse than for the Eulerian simulations due to the distorted computational mesh.

In Figure 8, the early stages of an ALE simulation at time $T = 0.1$ are presented for the same example. As we can see, the MOF results are best of all methods being compared, the multi-material interface smoothly transitions from the white-blue to the white-green interface and no major jumps appear. The results of VOF in correct ordering are comparable to the results of VOF with power diagrams at this early stage. We can observe minor material jumps and smoothness of the interface is violated. The worst results are clearly ob-

ACCEPTED MANUSCRIPT

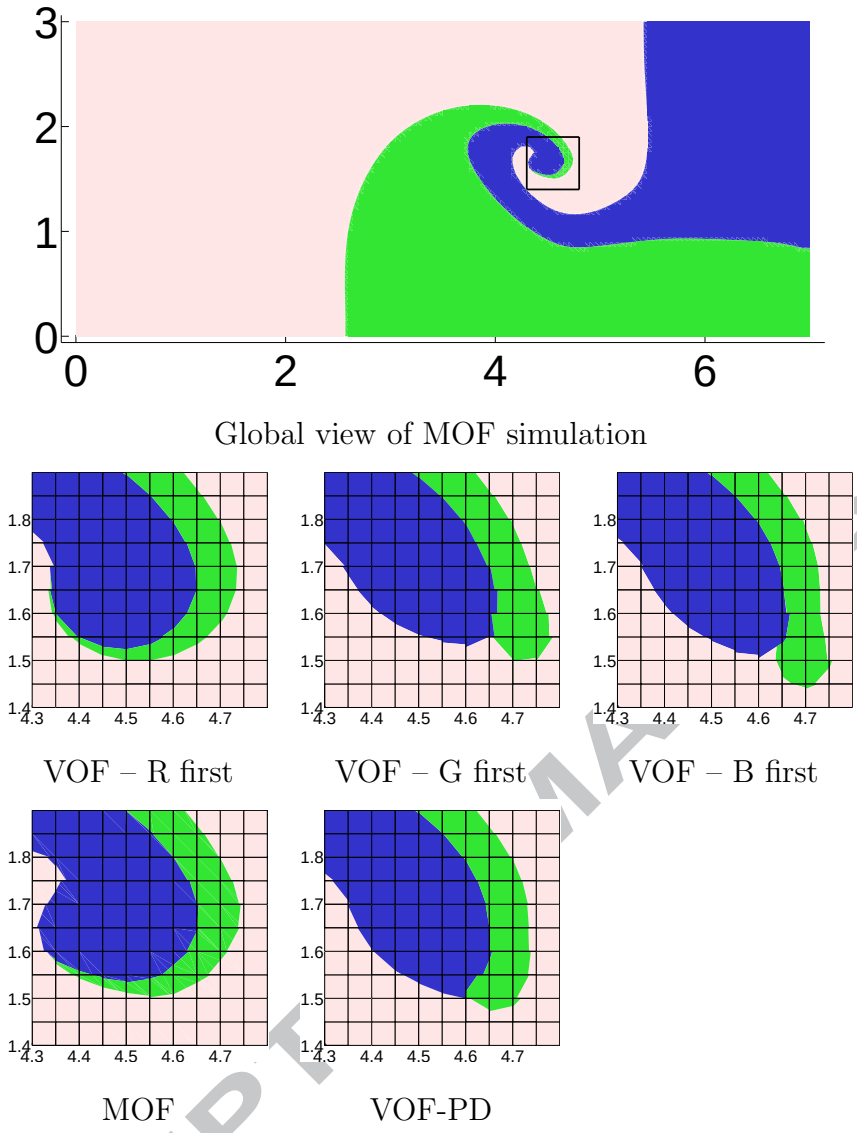

Fig. 7. Materials of triple point problem simulation, time $T = 5.0$. Eulerian runs (as Lagrangian step and remap to the initial orthogonal mesh) using different methods for material reconstruction are shown: global view on the entire computational domain for MOF method, and zooms to the three material junction for Youngs' VOF method (with different material orderings), MOF, and Power Diagram based methods are shown.

tained by VOF methods using the wrong material orderings. The T-shape of the interface is completely violated and an unphysical wedge of white material starts to separate blue and green materials, leading to more severe problems in later stages of the simulations.

Figure 9 presents results in the middle of the simulation ($T = 2.5$). In this time moment, the (initially orthogonal) computational mesh is already relatively distorted. As we can see, VOF in correct ordering resolves the longest green filament. Filament resolved by MOF is shorter, compact, with a relatively

ACCEPTED MANUSCRIPT

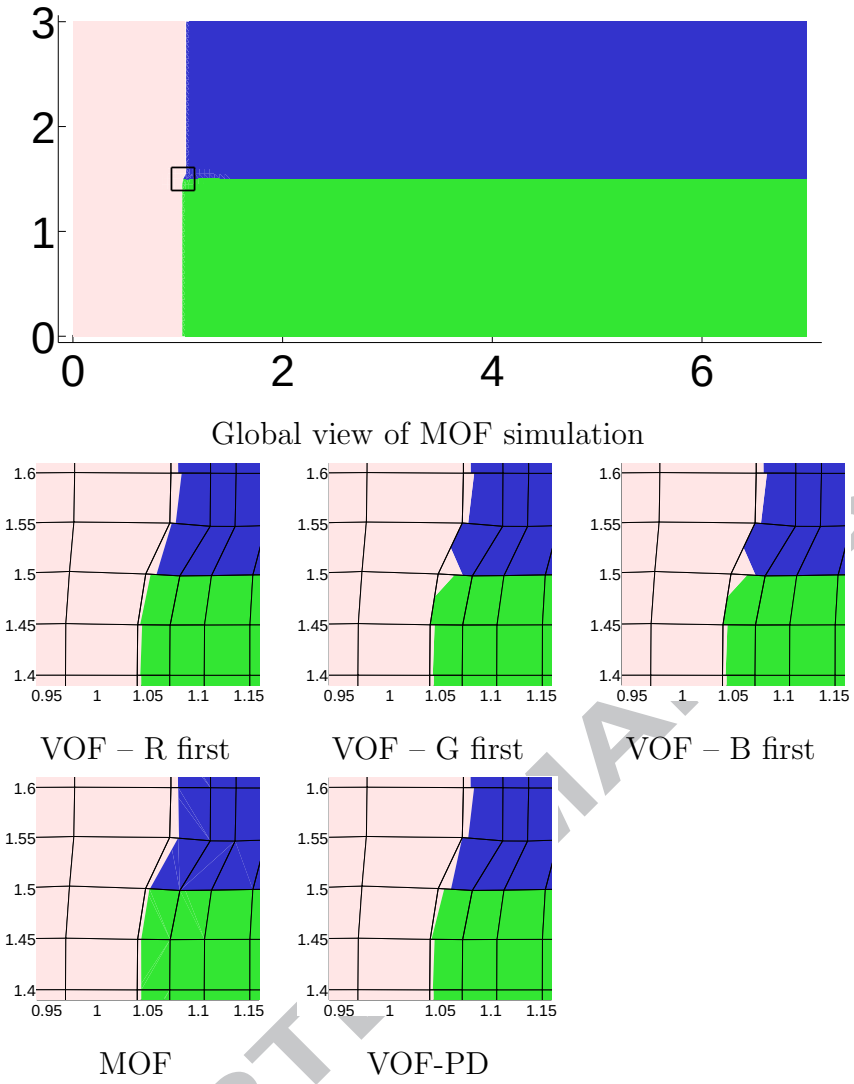

Fig. 8. Materials of triple point problem simulation, time $T = 0.1$. ALE runs (as Lagrangian step and remap to the Winslow smoothed mesh after every 20 Lagrangian steps) using different methods for material reconstruction are shown: global view on the entire computational domain for MOF method, and zooms to the three material junction for Youngs' VOF method (with different material orderings), MOF, and Power Diagram based methods are shown.

smooth interface. Power diagrams and VOF with wrong material orderings do not resolve the filament very well, but power diagrams surpass VOF with incorrect material order in material topology – no fragment of white and blue material appear on the other side of the green filament.

In Figure 10, we can see the last moment ($T = 5$) of the ALE simulation. MOF provides best result again – the filament is compact, relatively smooth, no separated tiny droplets are present. We can observe such small pieces for all VOF methods, even for correct ordering, where a tiny thin fiber of green material separates white-blue interface upto the picture boundary (zoomed in

ACCEPTED MANUSCRIPT

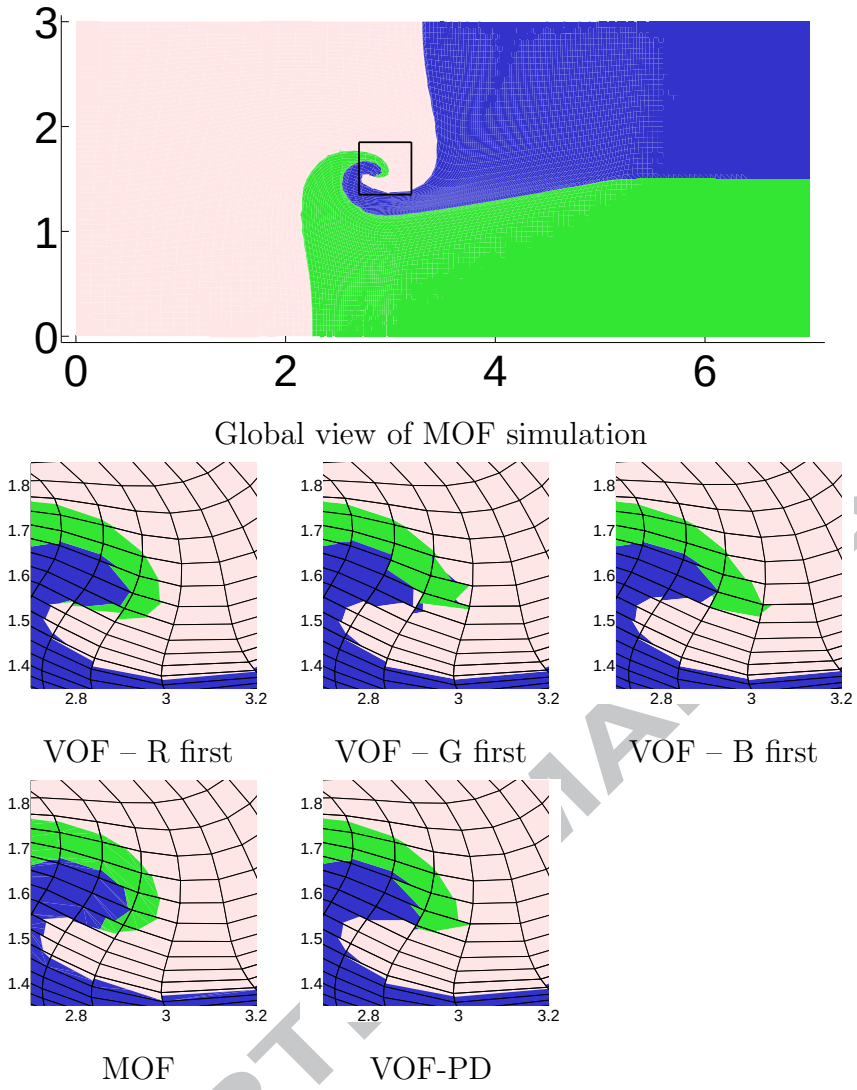

Fig. 9. Materials of triple point problem simulation, time $T = 2.5$. ALE runs (as Lagrangian step and remap to the Winslow smoothed mesh after every 20 Lagrangian steps) using different methods for material reconstruction are shown: global view on the entire computational domain for MOF method, and zooms to the three material junction for Youngs' VOF method (with different material orderings), MOF, and Power Diagram based methods are shown.

the last image of Figure 10). As for power diagrams, no droplets appear, but we can see that the green filament has broken into two parts.

6.2 Multi-material Sedov problem

The second numerical problem we present here is a multi-material generalization of the well known Sedov problem [31]. Typically, only one quarter of the Sedov problem is solved in the domain $\langle 0, 1.1\rangle^2$, final time of the simulation

ACCEPTED MANUSCRIPT

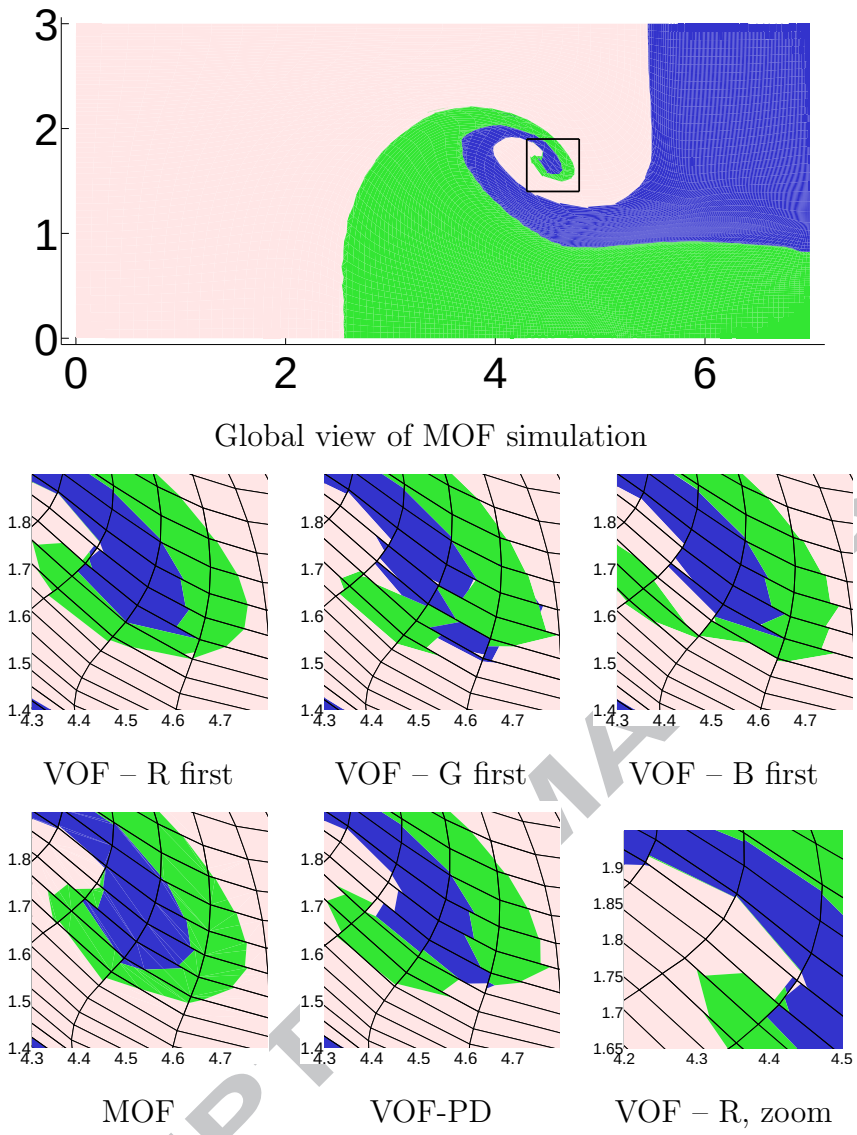

Fig. 10. Materials of triple point problem simulation, time $T = 5.0$. ALE runs (as Lagrangian step and remap to the Winslow smoothed mesh after every 20 Lagrangian steps) using different methods for material reconstruction are shown: global view on the entire computational domain for MOF method, and zooms to the three material junction for Youngs' VOF method (with different material orderings), MOF, and Power Diagram based methods are shown. A filament of green material for Youngs' VOF method with the correct material ordering is zoomed in the last image.

is $T = 1$. The standard Sedov problem has a uniform density $\rho = 1$, pressure $p = 10^{-6}$, and ratio of specific heats $\gamma = 1.4$, the fluid is static. A high energy cell in the domain origin is set, causing an explosion generating a strong circular shock wave spreading from the origin.

In our modification, we paint 4 materials over the Cartesian computational mesh containing 32^2 cells in the domain, as shown in Figure 11. The material

ACCEPTED MANUSCRIPT

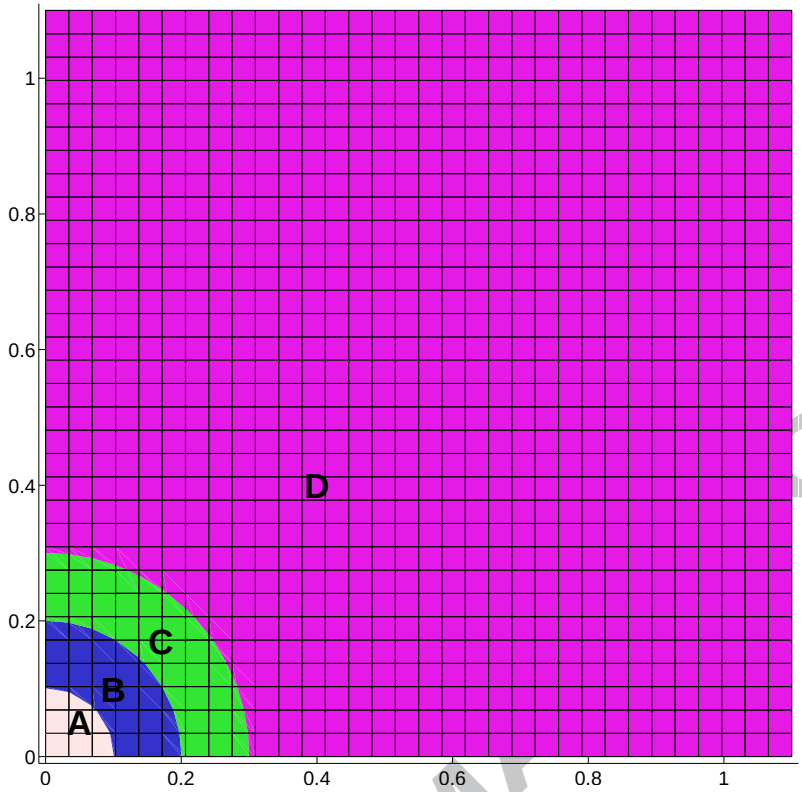

Fig. 11. Initial placement of materials for the multi-material Sedov problem painted onto a Cartesian 32^2 mesh. The material interfaces are placed at radiuses $r = 0.1$, $r = 0.2$, and $r = 0.3$.

interfaces are placed at radiuses $r = 0.1$, $r = 0.2$, and $r = 0.3$. The central material **A** represents the high-energy (and also high-density) material generating the explosion, its values are $\rho = 10$, $p = 163.88$, and $\gamma = 1.4$. The ring **B** has a very low density $\rho = 0.2$ and a very high ratio of specific heats $\gamma = 50$, which is the simplest approach for approximating a low-compressibility material. Pressure in ring **B** is $p = 10^{-6}$. The fluid values in the high-density ring **C** are $\rho = 5$, $p = 10^{-6}$, and $\gamma = 5/3$. Finally, in the rest of the domain **D**, the fluid values correspond to the values of a standard Sedov problem described before.

After the simulation starts, the explosion-generated shock wave compresses the low-density material **B**. As the density of the outer ring **C** is high, it has high momentum and is difficult to start moving, which causes even stronger compression of **B**. As the fluid moves outward from the explosion, material **B** is being extended. Due to its high γ, the material gets thiner instead of decreasing of its density. At the end of the simulation, the thickness of ring **B** changes to about 20% of its original thickness.

The simulation results for different material reconstruction methods using an ALE approach performing Winslow mesh smoothing and quantity remapping

ACCEPTED MANUSCRIPT

after every 10 Lagrangian steps are presented in Figure 12. For the Youngs'

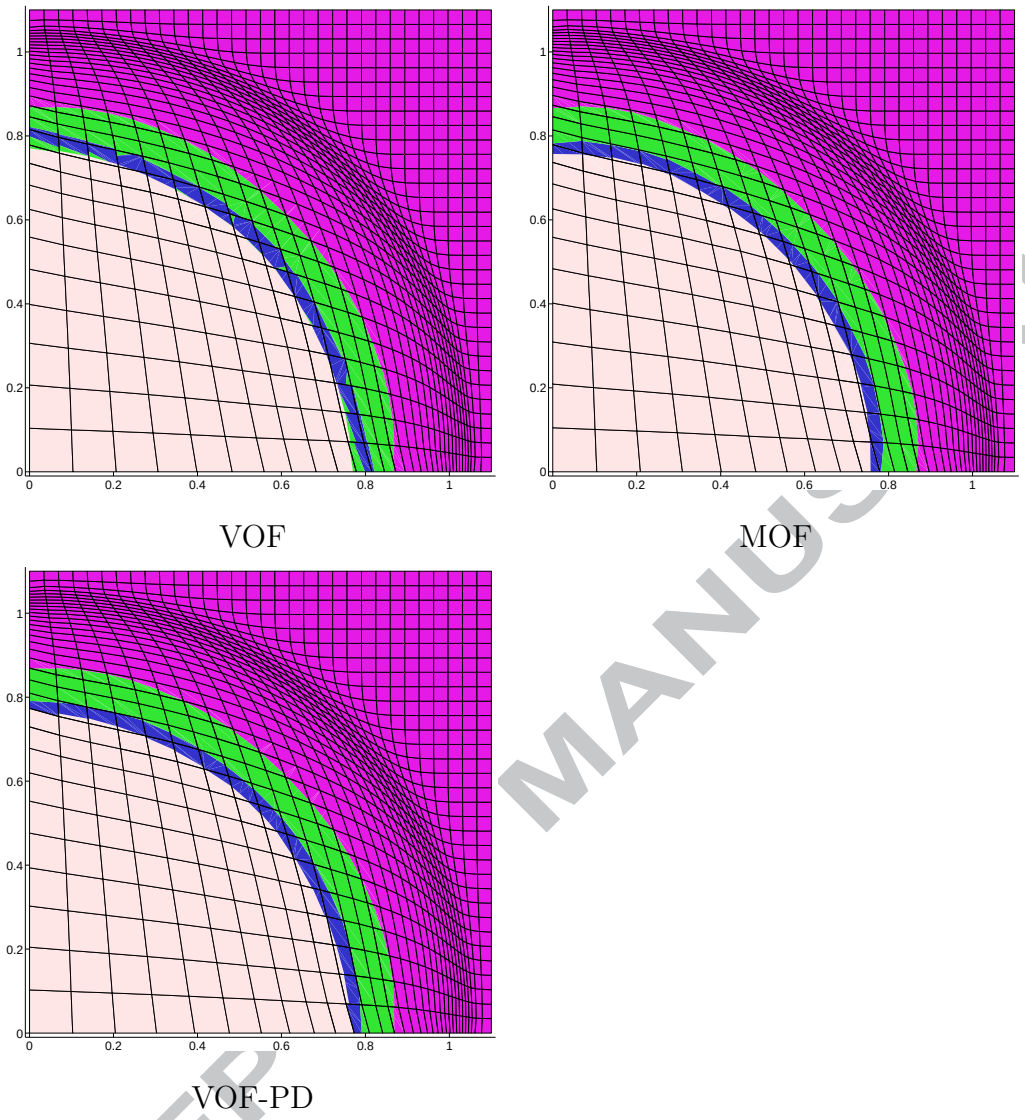

Fig. 12. Materials of multi-material Sedov problem, time $T = 1$, 32^2 mesh. ALE runs (as Lagrangian step and remap to the Winslow smoothed mesh after every 10 Lagrangian steps) using different methods for material reconstruction are shown: material interfaces for Youngs' VOF (in ABCD order), MOF, and Power Diagram based methods are shown.

VOF method, the **ABCD** ordering is used, which is considered to be correct for this problem (generally, for problems including layered structures, the ordering following the materials from one side to the other one is correct). Even so, the Youngs' VOF methods produces the worst results, and the blue ring **B** is broken at several places. As we can see, the severest material displacement is present at domain boundaries due to the distortion of the volume fraction gradient here. Although, we can also observe fragments of the green material between the red and blue ones along the whole blue ring. For MOF, the blue ring stays compact with smooth interfaces. For this problem, the results ob-

ACCEPTED MANUSCRIPT

tained by the Power Diagrams based VOF method are comparable to MOF results, with the exception of the inner material interface disturbances close to the domain boundary. These are again caused by the computation of the volume fraction gradient. Let us note, that the circular shock wave position is the same and is not influenced by the particular material reconstruction method.

6.3 Multi-material Saltzman-like Problem

The last problem we are going to discuss here is a modification of a standard Saltzman piston problem [32]. We use an orthogonal Cartesian 100×10 computational mesh in the computational domain $\langle -0.5, 0.5 \rangle \times \langle -0.05, 0.05 \rangle$. The standard Saltzman problem contains a uniform distribution of material density $\rho = 1$ and pressure $p = 2/3 \cdot 10^{-4}$ in the whole domain. The fluid is static and the ratio of specific heats is $\gamma = 5/3$. After the beginning of the simulation, the whole computational domain is compressed by a piston moving the left boundary with the unit velocity. As the simulations goes, a shock wave is formed in front of the piston, which passes the whole domain and reflects from the right boundary. It is possible to perform this simulation until quite a long time, when the shock wave reflects several times from the left and right boundaries. Let us note, that in time $T = 1$, the whole domain would be compressed to the 0 width, so this time is not reachable. This problem is often used for the investigation of the properties of Lagrangian solvers, especially when used in connection with an initially skewed computational mesh.

In our modification, we have placed several rings of different materials to the center of the computational domain, as can be seen in Figure 13. The ra-

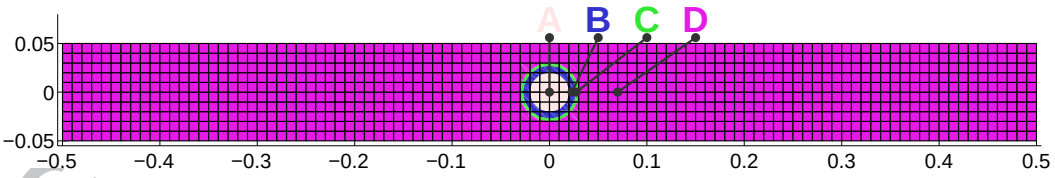

Fig. 13. Initial placement of materials for the multi-material Saltzman problem painted onto a Cartesian 100×10 mesh. The material interfaces are placed to the radiuses $r = 0.02$, $r = 0.027$, and $r = 0.03$.

diuses of the material interfaces are set to $r = 0.02$, $r = 0.027$, and $r = 0.03$. This problem is multi-material only formally, the fluid quantities of all materials are set to the same values as mentioned above. Therefore, the solution should exactly correspond to the 1D symmetric solution of the single-material problem.

In Figure 14, we can see the comparison of the Youngs' VOF, VOF-PD, and

ACCEPTED MANUSCRIPT

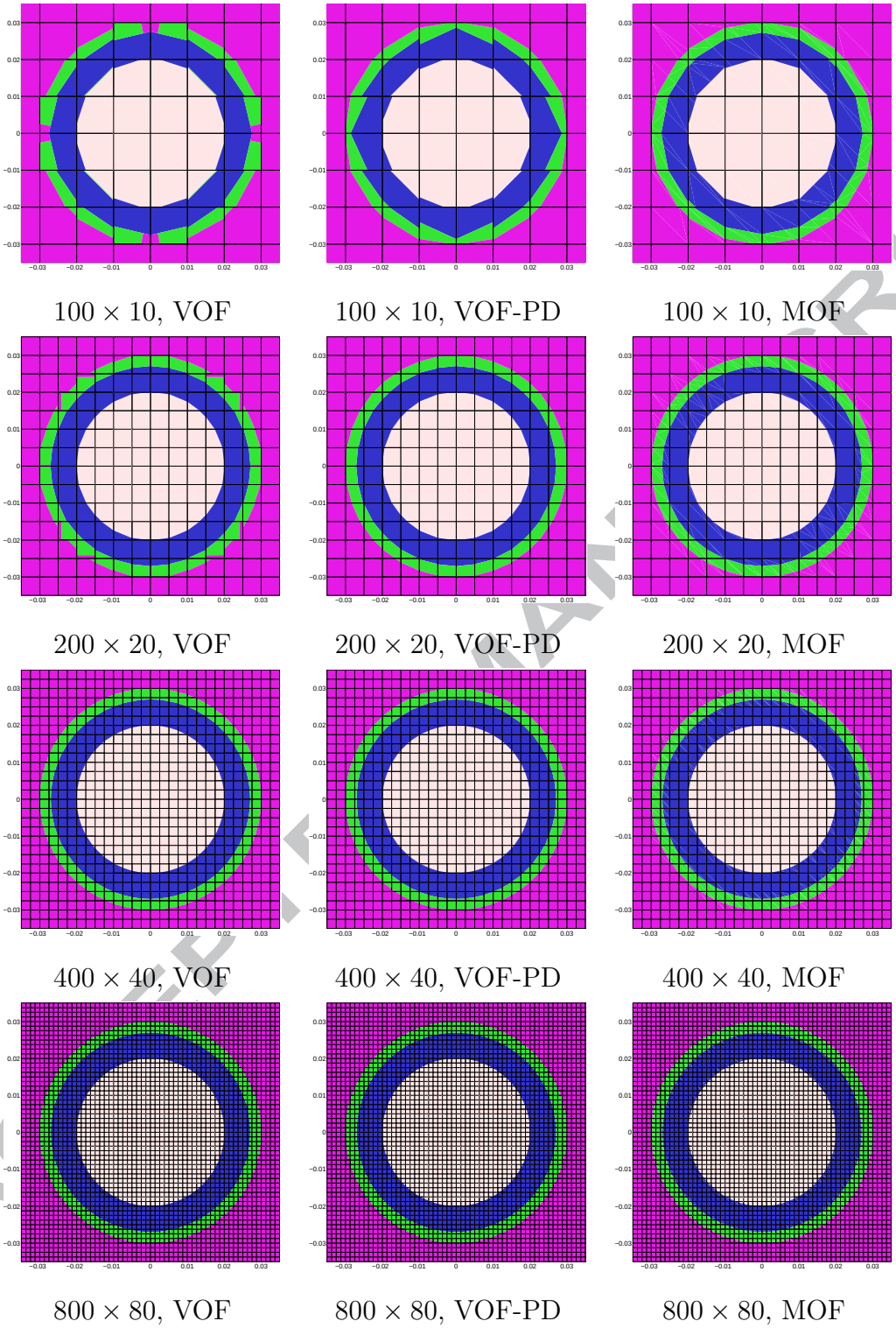

Fig. 14. Multi-material Saltzman problem in time $T = 0$ on a Cartesian meshes with different resolutions. The computational mesh and material polygons reconstructed by the different reconstruction methods in the ring regions are shown.

ACCEPTED MANUSCRIPT

MOF material reconstruction methods applied to the initial data of the described problem. For the Youngs' VOF methods, the **ABCD** material ordering was used, considered to the correct ordering for layered structures. The problem uses 100×10, 200×20, 400×40, and 800×80 mesh resolutions, in the images a zoom of the ring region is shown. For the lowest resolution, the problem is clearly under-resolved. We can observe severe distortions of the green ring due to inaccurate gradient computation. The gradient is computed by the Green-Gauss approach, and the stencil of the surrounding cells including the green material is not big enough for the filament structure to resolve the gradient accurately. We can even see pieces of the green material between the light-red and blue materials. The VOF-PD and MOF methods keep the material topology correctly, but the MOF method produces much smoother interfaces. The reason for non-smooth VOF-PD interfaces are the same as for the Youngs' VOF method – inaccurate gradient computation. For the 200×20 mesh, the situation is similar. We can still observe perturbances of the green ring material due to the inaccurate gradient computation. The MOF and VOF-PD results are now comparable, all interfaces are smooth. For the 400×40 mesh, few tiny magenta pieces can still be found between the blue and green rings in the case of VOF method. This can be seen in the zoom shown in Figure 15. Finally, for the highest resolution mesh 800×80, all

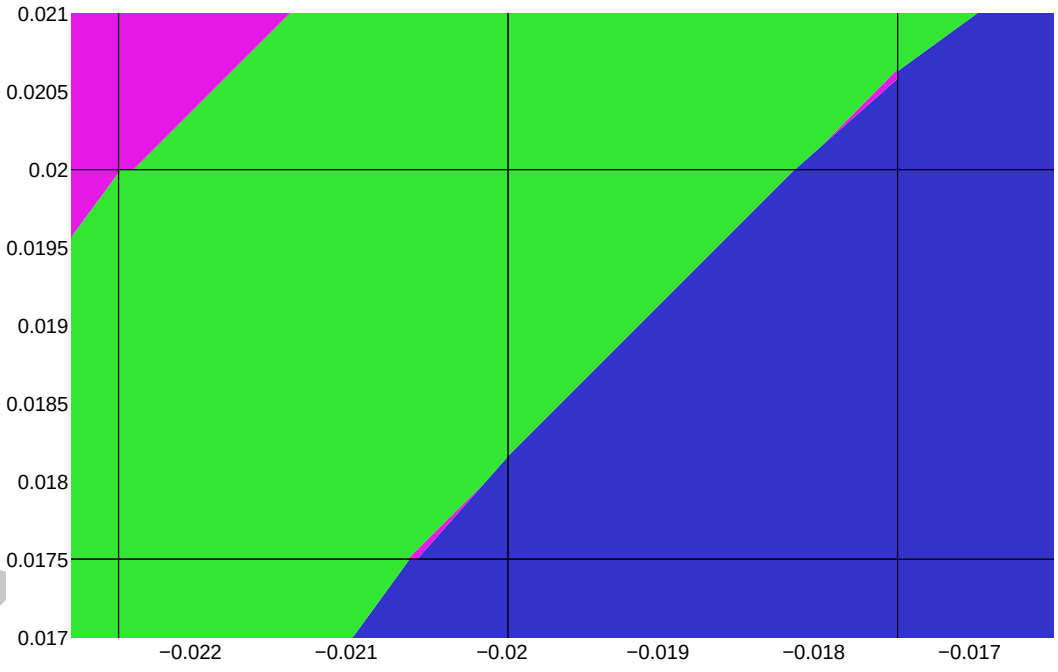

Fig. 15. Multi-material Saltzman problem in time $T = 0$ on a Cartesian 400×40 mesh. The computational mesh and material polygons reconstructed by the VOF reconstruction method are shown. Zoom shows fragments of the magenta material.

material features are at least 3 cells wide and all methods provide comparable results with smooth interfaces and correct material topology.

ACCEPTED MANUSCRIPT

Let us also note, that the problems with the Youngs' VOF method could be improved in this particular problem by changing the material ordering such that the thin green filament would be treated as last. As we have already said, generally for layered structures, the ordering respecting the ordering of the layers is considered as correct and used in most simulations. Moreover, this fix is not applicable if there would be two or more filaments next to each other.

We perform the simulation of the multi-material Saltzman-like problem till the (quite an early) final time $T = 0.6$, in which the shock wave passes the rings for the first time, as can be seen for the case of MOF method on the 100×10 mesh in Figure 16. As we can see, in this time the piston has reached

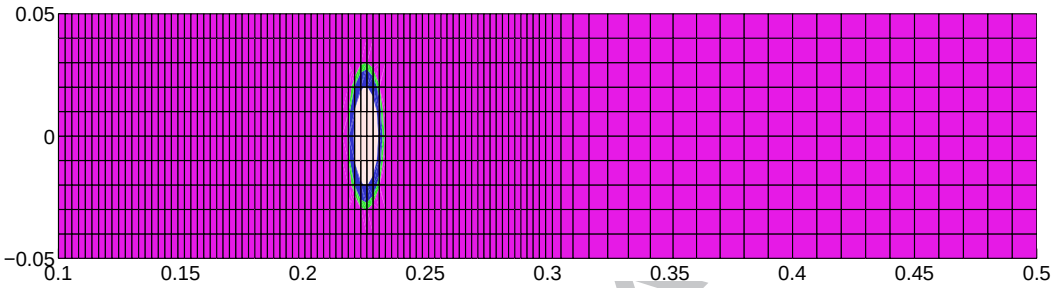

Fig. 16. Multi-material Saltzman problem in time $T = 0.6$ on a Cartesian 100×10 mesh obtained by the ALE1 simulation (Winslow mesh smoothing followed by the quantity remapping is performed after every single Lagrangian step). The computational mesh and material polygons reconstructed by the MOF reconstruction method are shown.

the position 0.1, the shock position is about 0.3. The left part of the domain (the part behind the shock wave, including the rings) is compressed and the computational cells have the aspect ratio of about 1/4. A zoom of the ring region is shown in Figure 17.

For comparison of different material reconstruction methods, see Figure 18. The images show zooms to the ring regions, the aspect ratio is not preserved here. As in Figure 14, the **ABCD** material ordering was used for the Youngs' VOF method. For the lowest 100×10 mesh resolution, both VOF and VOF-PD produce very bad results. VOF-PD surpasses the Youngs' VOF method slightly – the blue and green rings are mixed together, but stays relatively well separated from the background magenta material, contrary to the Youngs' VOF method for which all these three materials are mixed together. The problems of Youngs' VOF start in the very early stages of the simulations, as we saw in Figure 14. We can observe severe distortions of the thin green ring due to the Green-Gauss computation of the material volume fraction gradient in the coarse mesh. Despite the coarseness of the mesh the MOF result is superior. For the finer 200×20 computational mesh, the Youngs' VOF method (with the correct material ordering) is the worst – the green ring is completely distorted, and we can see small pieces of the green and magenta materials

ACCEPTED MANUSCRIPT

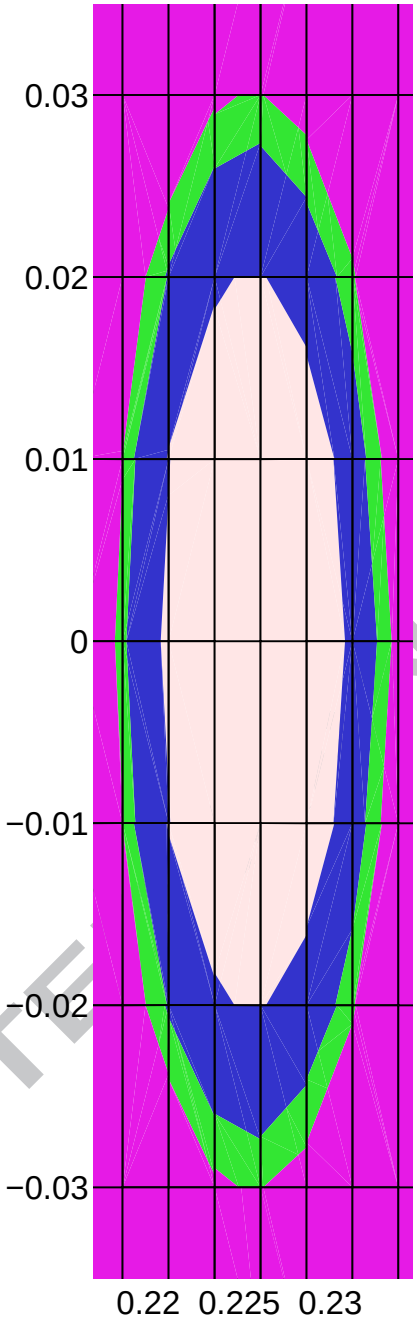

Fig. 17. Zoom-in of the multi-material Saltzman problem in time $T = 0.6$ on a Cartesian 100×10 mesh obtained by the ALE1 simulation (Winslow mesh smoothing followed by the quantity remapping is performed after every single Lagrangian step). The computational mesh and material polygons reconstructed by the MOF reconstruction method are shown.

on the blue-light red interface. The VOF-PD result is significantly better, the green ring is much more compact, but still small pieces of the magenta and blue materials can be found inside the left and right parts of the green circle. For MOF, all materials stay compact and no problems with the tiny material pieces appear. In the case of 400×40 mesh resolution, the VOF method provides

ACCEPTED MANUSCRIPT

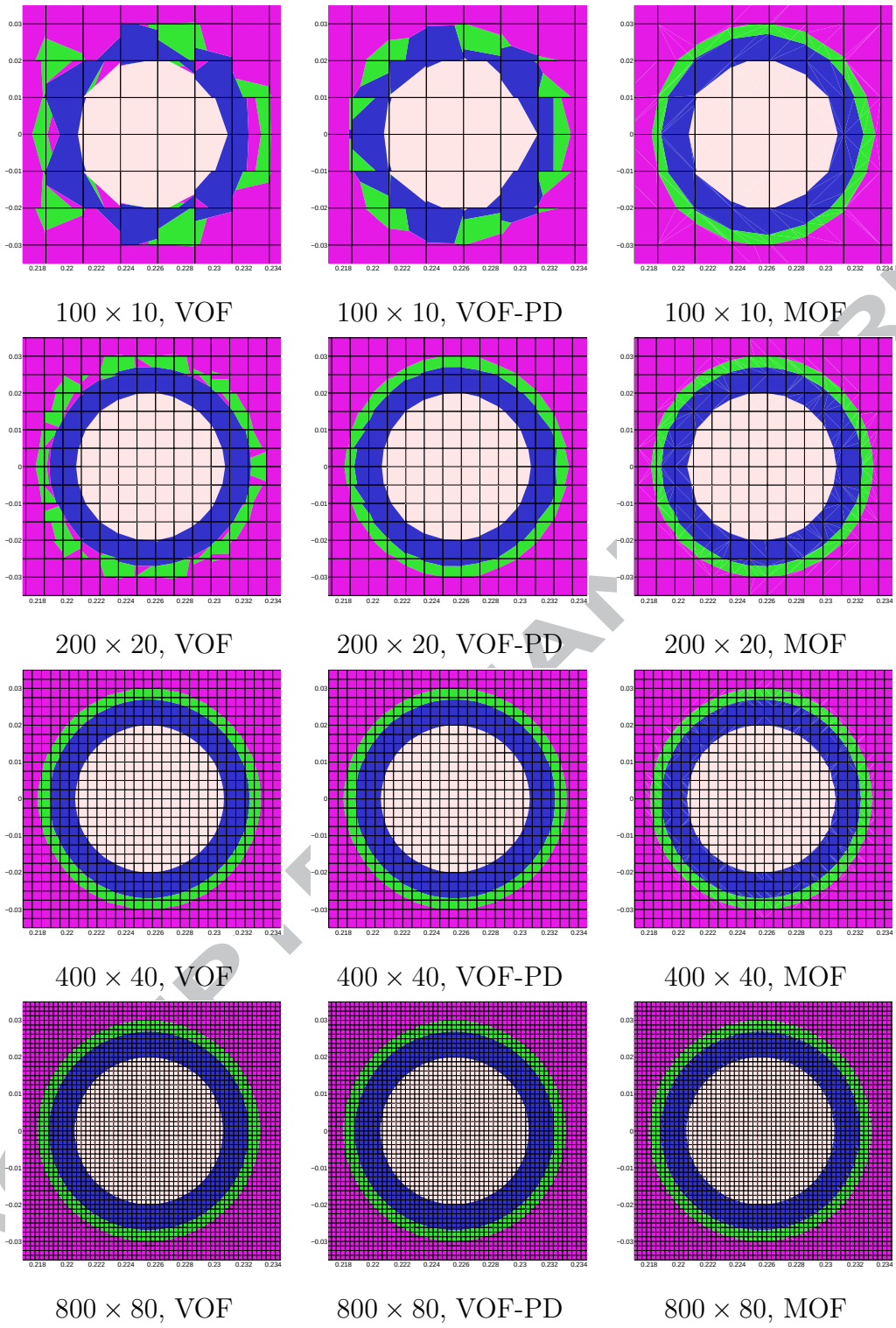

Fig. 18. Multi-material Saltzman problem in time $T = 0.6$ on a Cartesian meshes with different resolutions, obtained by the ALE1 simulation (Winslow mesh smoothing followed by the quantity remapping is performed after every single Lagrangian step). The computational mesh and material polygons reconstructed by the different reconstruction methods in the ring regions are shown.

ACCEPTED MANUSCRIPT

better results than in the lower resolutions, but there are still fragments of the magenta material between the green and blue rings. We do not observe any material topology problems with VOF-PD or MOF method. Finally, the same set of simulations was performed on the finest 800×80 mesh. As we can see, even the thinnest green ring is now about 3 cells wide. This allow an exact computation of the gradient of the volume fractions functions, and so the final materials are smooth, compact, and comparable to the results of the MOF method. Similarly, VOF-PD results are comparable to MOF results, materials are smooth, and no problems with material topology are visible. As we can see, all methods converge towards the same material distribution as the mesh refines.

7 Conclusions

We have presented a comparison of a material-order-dependent VOF method, a material-order-independent VOF method and a material-order-independent MOF method for a complex compressible flow involving more than two materials.

From the simulations that we have run, we conclude that:

- MOF performs the most accurate reconstructions, generally capturing filaments accurately and getting the material topology correct. Since MOF is quite recent it generally does not exist in many codes. Therefore, this method is the best choice when developing new flow codes or when revamping the interface tracking machinery. It is not advisable to introduce MOF reconstruction into a flow code without ensuring that the advection (remapping) of centroids is done accurately through overlays (exact, intersection-based remapping method).
- VOF with the correct material order performs remarkably well although the resolution of filaments and other small features is poorer than MOF. Since VOF commonly exists in flow codes that perform this type of interface tracking, it is a natural choice when the flow is simple and the material order can be predicted quite easily. It is also a good choice when the flow has only two materials and no filamentary or other structures smaller than 3-4 times the grid resolution are expected.
- Compared to VOF, the MOF method is less efficient. As it was already mentioned, all possible material combinations are tested to find the optimal material placement. If the number of materials in one cell would happen to be high (more than 5) in many cells, the MOF method could represent a considerable computational cost of the simulation. Fortunately, in the usual simulations, this situation is very rare – typically, there are many 2-material cells, some 3-material cells, and just a few 4 or more -material cells.

ACCEPTED MANUSCRIPT

- VOF with power diagrams performs more poorly than MOF or VOF with the right material order but usually gets the interface topology right. This method is a good choice when the advection machinery cannot be revamped to perform overlays but the interface reconstruction can be rewritten simply to partition cells using the power diagram.
- VOF with the wrong order performs poorly even for simple flows and is not advised. If the ordering cannot be predicted or enforced strictly, it is better to use VOF with the power diagram reconstruction.

A Appendix

A.1 Lagrangian update of material centroids

The Lagrangian step may be viewed as the implicit creation of a family of maps, $\phi^n(\mathbf{x}) : \mathbb{R}^d \mapsto \mathbb{R}^d$, such that $\mathbf{x}^{n+1} = \phi^{n+1}(\mathbf{x}^n)$. Any material region, $\Omega^t \subset \mathbb{R}^d$, evolves over a time step as

$$\Omega^{n+1} = \phi^{n+1}(\Omega^n) \tag{A.1}$$

The map ϕ^{n+1} is illustrated in Figure A.1.

If the map is an affine transformation, that is

$$\phi^{n+1}(\mathbf{x}) = A\mathbf{x} + \mathbf{b} \tag{A.2}$$

where $A \in \mathbb{R}^{d\times d}$ is invertible and $\mathbf{b} \in \mathbb{R}^d$, then if $\mathbf{x}_c(\Omega^n)$ is the centroid of the region and $\Omega^{n+1} = \phi^{n+1}(\Omega^n)$, then $\mathbf{x}_c(\Omega^{n+1}) = A\mathbf{x}_c(\Omega^n) + b$. That is, the transformed centroid is the centroid of the transformed region.

To demonstrate this,

$$\begin{aligned}\|\Omega^{n+1}\|\mathbf{x}_c(\Omega^{n+1}) &= \int_{\Omega^{n+1}} \mathbf{x}\, dx \\ &= \int_{\Omega^n} (A\mathbf{y} + b)\det A\, dy \\ &= (\det A)\|\Omega^n\|A\mathbf{x}_c(\Omega^n) + \mathbf{b}(\det A)\|\Omega^n\|\end{aligned}$$

Noting that

$$\|\Omega^{n+1}\| = \int_{\Omega^{n+1}} dx = \int_{\Omega^n} \det A\, dx = \|\Omega^n\|\det A$$

we obtain,

$$\mathbf{x}_c(\Omega^{n+1}) = A\mathbf{x}_c(\Omega^n) + b$$

ACCEPTED MANUSCRIPT

The actual Lagrangian evolution of the region is given by the pointwise equation

$$\frac{d\mathbf{x}}{dt} = \mathbf{u}(\mathbf{x}, t) \quad \forall \mathbf{x} \in \Omega^t \tag{A.3}$$

assuming the velocity field is known. The transformation, ϕ^{n+1}, is then the solution to Equation A.3 over the time interval $[t^n, t^{n+1}]$.

With sufficient regularity, the velocity field can be expanded as

$$u_j(\mathbf{x}, t) = u_j(\mathbf{x}_0, t^n) + (t - t^n)\frac{\partial u_j(\mathbf{x}_0, t^n)}{\partial t} + (x_i - x_i^0)\frac{\partial u_j(\mathbf{x}_0, t^n)}{\partial x_i} + \mathcal{O}(\Delta x^2) + \mathcal{O}(\Delta t^2) + \mathcal{O}(\Delta x \Delta t). \tag{A.4}$$

Substituting this into Equation A.3 and integrating, we find that

$$\phi^{n+1}(\mathbf{x}) = \mathbf{x} + \mathbf{u}(x_0, t^n)\Delta t + \mathcal{O}(\Delta t^2) + \mathcal{O}(\Delta t \Delta x). \tag{A.5}$$

Assuming $\Delta t \approx \Delta x$, then the transformation defining the Lagrangian evolution over a time step may be approximated as an affine transformation with second order accuracy.

A.2 Constant parametric coordinate method

A method for updating material centroids during a Lagrangian step can exploit this implicit evolution operator described above. The method described [2,19] is based on the existence of a mapping of the computational cell to and from a logical space. It is assumed that the centroid of the material region has the same logical coordinates, before and after the Lagrangian motion of the cell. To obtain the centroid after the Lagrangian motion, the logical coordinates of the centroid at the previous step are given to the logical to physical mapping corresponding to the cell after the motion. This process is illustrated in Figure A.1. It is important to note that the logical to physical space mapping is different for each time step and the cells evolve in time.

The accuracy of the method relies on the properties of the logical to physical coordinate transformations used.

Assume each cell has local coordinates, $\mathbf{r} \in S$, with an invertible map into physical coordinates, $\psi^n : S \mapsto \Omega^n$.

We define a family of local parameterizations, $\{\psi^n\}$ to be **linearity preserving**, if points from the parametric space, S, are mapped such that if

$$\mathbf{x}^{n+1} = A\mathbf{x}^n + b, \tag{A.6}$$

ACCEPTED MANUSCRIPT

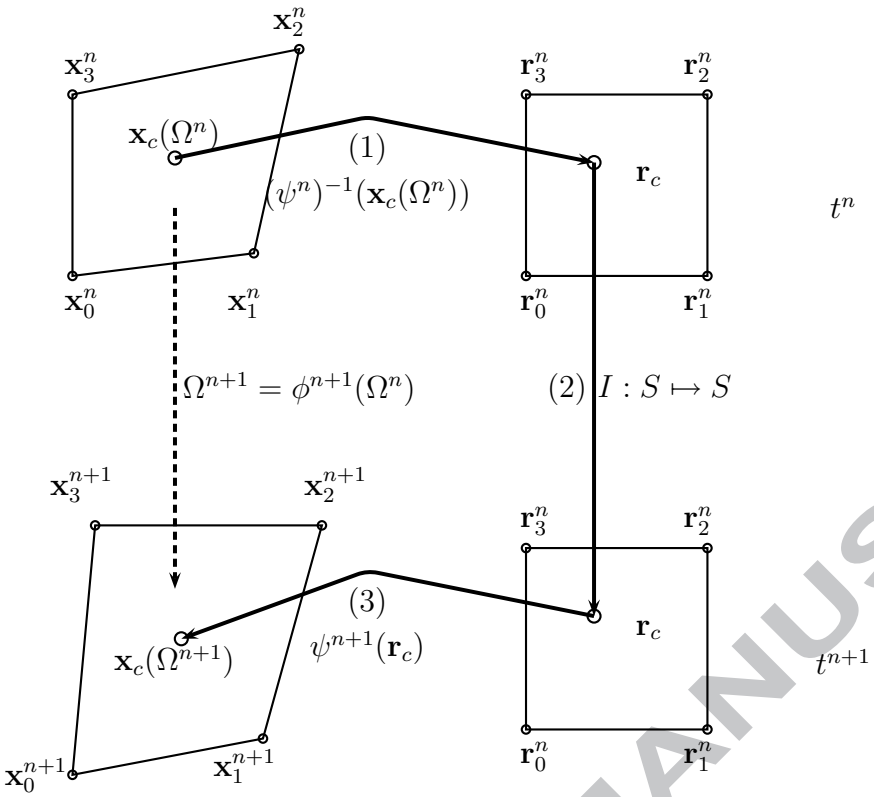

Fig. A.1. Steps in the constant parametric coordinate method. (1) The logical coordinates of the centroid at time t^n are calculated. (2) It is assumed the centroid has the same logical coordinates at time t^{n+1}. (3) The logical coordinates are mapped to physical coordinates to give the location. This gives a second order accurate approximation to the centroid of the evolved region $\Omega^{n+1} = \phi^{n+1}(\Omega^n)$.

then if $\mathbf{x}^n = \psi^n(\mathbf{r})$,

$$\mathbf{x}^{n+1} = \psi^{n+1}(\mathbf{r}) = A\psi^n(\mathbf{r}) + b = A\mathbf{x}^n + \mathbf{b} \tag{A.7}$$

Equivalently,

$$\psi^{n+1} = A\psi^n + \mathbf{b} \tag{A.8}$$

The bilinear parameterization of quads satisfies this property: the two orthogonal coordinates, $(r, s) \in [0, 1]^2$ linearly interpolate the vertices (see Figure A.1 for node numbering)

$$\psi^n(r, s) = (1 - r)\left[(1 - s)\mathbf{x}_0^n + s\mathbf{x}_3^n\right] + r\left[(1 - s)\mathbf{x}_1^n + s\mathbf{x}_2^n\right] \tag{A.9}$$

Clearly, $\psi^{n+1} = A\psi^n + \mathbf{b}$ as $\mathbf{x_j}^{n+1} = A\mathbf{x_j}^n + \mathbf{b}$ for $j = 0, \ldots, 3$.

The generalized barycentric coordinates of polygon with vertices $\{\mathbf{v}_i\}$ also satisfies the linearity preserving property. To demonstrate this, barycentric coordinates satisfy the properties [33],

ACCEPTED MANUSCRIPT

$$\mathbf{x} = \sum_i \lambda_i \mathbf{v}_i = \psi^n(\lambda), \tag{A.10}$$

$$\sum_i \lambda_i = 1, \tag{A.11}$$

$$\lambda_i \geq 0. \tag{A.12}$$

If $\mathbf{x}$ has barycentric coordinates λ, then if $\mathbf{x}^n = \psi^n(\lambda)$,

$$A\mathbf{x} = \sum_i \lambda_i A\mathbf{v}_i \tag{A.13}$$

$$A\psi^n(\lambda) + \mathbf{b} = \sum_i \lambda_i A\mathbf{v}_i + \mathbf{b}\sum_i \lambda_i \tag{A.14}$$

$$A\psi^n(\lambda) + \mathbf{b} = \sum_i \lambda_i (A\mathbf{v}_i + \mathbf{b}) = \psi^{n+1}(\lambda) \tag{A.15}$$

where $\sum_i \lambda_i = 1$ was utilized in the second step.

If the family of transformations satisfy the linearity preserving property, then we may analyze the accuracy of the constant parametric coordinate method. If the parameterization family, $\{\psi^n\}$, is linearity preserving, then updating the location of a material centroid by assuming its parametric coordinates are unchanged is exact for linear motions, since for an arbitrary subdomain mapped with an affine transformation,

$$\mathbf{x}_c(\Omega^{n+1}) = A\mathbf{x}_c(\Omega^n) + b \tag{A.16}$$

If the transformation is linearity preserving, then

$$\mathbf{x}_c(\Omega^{n+1}) = \varphi^{n+1}(\mathbf{r}) = A\varphi^n(\mathbf{r}) + b = A\mathbf{x}_c(\Omega^n) + b \tag{A.17}$$

In general, the Lagrangian motion will not be linear. However, as was shown in the previous section, for sufficient regularity in time an affine approximation to the Lagrangian motion is second order accurate.

Acknowledgments

This work was performed under the auspices of the National Nuclear Security Administration of the US Department of Energy at Los Alamos National Laboratory under Contract No. DE-AC52-06NA25396 and supported by the DOE Advanced Simulation and Computing (ASC) program. The authors acknowledge the partial support of the DOE Office of Science ASCR Program.

ACCEPTED MANUSCRIPT

References

[1] Benson DJ. Computational methods in Lagrangian and Eulerian hydrocodes. *Computer Methods in Applied Mechanics and Engineering* 1992; **99**: 235-394.

[2] Benson DJ. Volume of fluid interface reconstruction methods for multi-material problems. *Applied Mechanics Review* 2002; **55**(2): 151-165.

[3] Rider WJ, Kothe DB. Reconstructing volume tracking. *Journal of Computational Physics* 1998; **141**: 112-152.

[4] Scardovelli R, Zaleski S. Direct numerical simulation of free-surface and interfacial flow. *Annual Review of Fluid Mechanics* 1999; **31**: 567-603.

[5] Hirt CW, Nichols BD. Volume of fluid (VOF) method for the dynamics of free boundaries. *Journal of Computational Physics* 1981; **39**: 201-225.

[6] Dyadechko V, Shashkov MJ. Reconstruction of multi-material interfaces from moment data. *Journal of Computational Physics*, 2008; **11**: 5361-5384.

[7] Noh WF, Woodward P. SLIC (simple line interface calculation). In van der Vooren AI and Zandbergen PJ, editors, *5th International Conference on Numerical Methods in Fluid Dynamics*, pages 330-340. Springer-Verlag, 1976.

[8] Youngs DL. Time dependent multi-material flow with large fluid distortion. In K. W. Morton and M. J. Baines, editors, *Numerical Methods for Fluid Dynamics*, pages 273-285. Academic Press, 1982.

[9] Youngs DL. An interface tracking method for a 3D Eulerian hydrodynamics code. Technical Report AWE/44/92/35, AWRE Design and Math Division, 1984.

[10] Pilliod JE Jr., Puckett EG. Second-order accurate volume-of-fluid algorithms for tracking material interfaces. *Journal of Computational Physics* 2004; **199**: 465-502.

[11] Swartz BK. The second-order sharpening of blurred smooth borders. *Mathematics of Computation* 1989; **52**(186): 675-714.

[12] Steinhaus H. A note on the ham sandwich theorem *Mathesis Polska*, 1938; **9**: 26-28.

[13] Stone AH, Tukey JW. Generalized "sandwich" theorems *Duke Mathematical Journal*, 1942; **9**: 356-359.

[14] Mosso S, Clancy S. A geometrically derived priority system for Young's interface reconstruction. Technical Report LA-CP-95-0081, Los Alamos National Laboratory, Los Alamos, NM, 1995.

[15] Garimella RV, Dyadechko V, Swartz BK, Shaskov MJ. Interface reconstruction in multi-fluid, multi-phase flow simulations. In *Proceedings of the 14th International Meshing Roundtable*, pages 19-32, San Diego, CA, September 2005. Springer.

ACCEPTED MANUSCRIPT

[16] Schofield SP, Garimella RV, Francois MM, Loubere R. Material order-independent interface reconstruction using power diagrams *International Journal for Numerical Methods in Fluids*, 2007; **56**(6): 643-659.

[17] Ahn HT, Shashkov M. Multi-material interface reconstruction on generalized polyhedral meshes. *Journal of Computational Physics* 2007; **226**: 2096-2132.

[18] Schofield SP, Garimella RV, Francois MM, Loubere R. A second-order accurate material-order-independent interface reconstruction technique for multi-material flow simulations *Journal of Computational Physics*, 2009; **228**(3): 731-745.

[19] Benson DJ. Eulerian finite element methods for the micromechanics of heterogeneous materials: Dynamic prioritization of material interfaces. *Computer Methods in Applied Mechanics and Engineering*, 1998, **151**: 343-360.

[20] Aurenhammer F. Power diagrams: properties, algorithms and applications. *SIAM J. Computing* 1987; **16**(1): 78-96.

[21] Imai H, Iri M, Murota K. Voronoi diagram in the Laguerre geometry and its applications. *SIAM J. Computing* 1985; **14**(1): 93-105.

[22] Caramana EJ, Burton DE, Shashkov MJ, Whalen PP. The construction of compatible hydrodynamics algorithms utilizing conservation of total energy. *Journal of Computational Physics* 1998; **146**: 227-262.

[23] Caramana EJ, Shashkov MJ, Whalen PP. Formulations of artificial viscosity for muti-dimensional shock wave computations. *Journal of Computational Physics* 1998; **144**: 70-97.

[24] Scovazzi G, Love E, Shashkov M. Multi-scale Lagrangian shock hydrodynamics on Q1/P0 finite elements: Theoretical framework and two-dimensional computations. *Comput. Methods Appl. Mech. Engrg.* 2008; **197**: 1056-1079.

[25] Shashkov M. Closure models for multidimensional cells in arbitrary Lagrangian-Eulerian hydrocodes. *Int. J. Numer. Meth. Fluids* 2008; **56**: 1497-1504.

[26] Winslow AM. Equipotential zoning of two-dimensional meshes. Technical Report UCRL-7312, Lawrence Livermore National Laboratory, 1963.

[27] Margolin LG, Shashkov M. Second-order sign-preserving conservative interpolation (remapping) on general grids. *Journal of Computational Physics* 2003; **184**: 266-298.

[28] Pember RB, Anderson RW. A comparison of staggered-mesh Lagrange plus remap and cell-centered direct Eulerian Godunov schemes for Eulerian shock hydrodynamics. Technical Report UCRL-JC-139820, Lawrence Livermore National Laboratory, 2000.

[29] Kucharik M, Shashkov M. Conservative Multi-Material Remap for Staggered Discretization. *In preparation* 2009.

[30] Maire P-H. Personal Communication. Los Alamos National Laboratory, 2007.

ACCEPTED MANUSCRIPT

[31] Sedov LI. Similarity and Dimensional Methods in Mechanics. Academic Press, 1959.

[32] Dukowicz JK, Meltz BJA. Vorticity errors in multidimensional Lagrangian codes. *Journal of Computational Physics*, 1992; **99**(1): 115-134.

[33] J. Warren, S. Schaefer, A. N. Hirani, and M. Desbrun. Barycentric coordinates for convex sets. *Advances in Computational Mathematics*, 2007; **27**(3): 319-338.

ACCEPTED MANUSCRIPT